Deutscher Luft- und Raumfahrtkongress 2008
DocumentID: 81212

NUMERICAL INVESTIGATION OF THE FLOW IN THE SUPERSONIC COMBUSTION CHAMBER OF THE ITLR AND COMPARISON WITH EXPERIMENTAL DATA

M.C. Banica, T. Scheuermann, J. Chun, B. Weigand, and J.v. Wolfersdorf
Universität Stuttgart,Institut für Thermodynamik der Luft- und Raumfahrt (ITLR),
Pfaffenwaldring 31, 70569 Stuttgart, Germany

Abstract

Space transportation systems based on scramjet propulsion have the potential to significantly decrease the costs for access to space. However, substantial obstacles still exist in realizing such systems. Experiments in the relevant Mach number regime are difficult to perform and flight tests are very expensive. Numerical methods are very valuable for system layout in these cases. For the present investigation, we use the commercial code CFD++, which we validate against experimental data for hydrogen combustion in the supersonic combustion chamber of the Institute of Aerospace Thermodynamics (ITLR) at the Universität Stuttgart. Hydrogen is injected by means of a three dimensional lobed strut injector. Our numerical data matches the experiments reasonably well. We investigate the effects of varying equivalence ratios, total pressures, injection Mach numbers and wall temperatures. In addition, we determine the limits for weak combustion and thermal choking. Recirculation regions develop on the channel walls in the immediate vicinity of the injector. Hot combustion products are found in the vicinity of both the chamber walls and the trailing edges of the injector. This leads to high heat loads. Injection of additional hydrogen can reduce these but has negative effects on burnout ratios. The hydrogen-air mixture ignites at the trailing edges of the injector. Approximately 90% of the hydrogen is consumed within a distance of six channel heights after injection.

1 INTRODUCTION

Several ongoing research efforts to develop a scramjet powered flight vehicle in Australia, Europe, Russia and the USA, among others, clearly demonstrate the increasing interest in this key technology. Scramjet powered vehicles have the potential to decrease the costs of access to space by increasing payloads, lowering turn-around times and employing reusable plane-type layouts that can operate from airport-like bases. However, the technological challenges involved in developing such a system are demanding. For example, flight experiments are very costly and there are no experimental facilities known to the authors that can operate continuously at the total temperatures and total pressures required to simulate actual flight conditions. In addition, an operational system has to cover a wide range of flight Mach numbers which requires the engines to allow at least dual-mode operation. Finally, there are unresolved questions regarding the thermal protection system, the cooling, the flight control systems and others. The present investigation was carried out within the framework of a national research effort to layout a scramjet propulsion system. This project is described in more detail by Weigand et al. [1]. In the following, we present numerical data on the fluid dynamical processes in our in-house supersonic combustion facility and validate them, where possible, against experimental results. The validation step is particularly important since it allows us to estimate how well the numerical method will be able to predict operating points outside the operating limits that are set by the experimental facilities. We vary several parameters and find that we can reproduce all combustion modes, i.e. strong combustion, weak combustion, thermal choking and blow off. Strong combustion is the desired operation mode under flight conditions. Here, the flame is attached to or is in close proximity to the trailing edges of the injector. Burnout ratios and hence combustion efficiencies are high. Weak combustion is characterized by a shock train that develops in the diverging part of the channel. It is caused by an overexpansion of the flow when atmospheric back pressure is imposed at the channel exit. The rising static temperatures lead to ignition of the fuel-air mixture in this shock system. If the back pressure is lowered to sufficiently low values, the combustion process ceases. This situation is referred to as blow off. Finally, if too much fuel is injected, the flow becomes thermally choked. This leads to the development of a shock system upstream of the injection point which decelerates the flow to subsonic speeds and causes significant losses in total pressure. For a given geometry, the combustion mode is determined by the equivalence ratio and the stagnation properties of the air flow. Strong combustion and weak combustion are also described in more detail by Chun et al. [2].

2 COMBUSTION CHAMBER

The combustion chamber is schematically shown in figure 1. It has a rectangular cross section of width 40mm and a height at isolator exit h=35.4mm. The figure represents a cut through the symmetry plane.

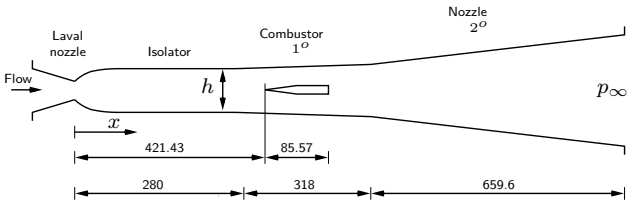

Figure 1: Experimental facility, lengths in [mm]

Flow enters the chamber through the Laval nozzle which accelerates it to a Mach number of M=2.1. As usual, the isolator is required to prevent any back-reaction of the combustion process on the inflow. The combustor has an opening angle of 1^o and is followed by a diverging part with an opening angle of 2^o. The flow exits into ambient conditions where $p_\infty = 0.96$bar. Downstream distance, x, is measured from the throat of the Laval nozzle where $x = 0$. The chamber components have the positions and lengths given in figure 1. The facility is designed for continuous operation and can provide a maximum total temperature of $T_{0,air,max} = 1500$K and a maximum total pressure of $p_{0,air,max} = 10$bar. Experimental data is collected by measuring static wall pressure distributions in the symmetry plane on the upper wall. This data is compared with numerical results. A more detailed description of the setup is given by Chun et al. [2].

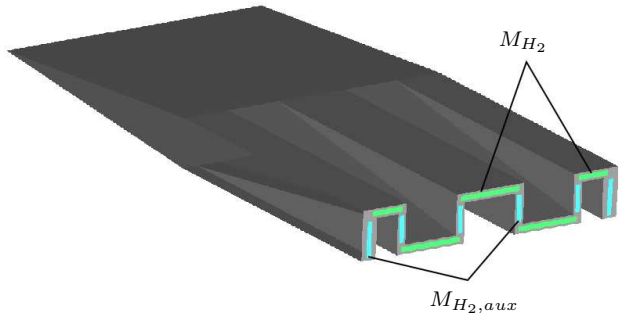

Figure 2: Schematic view of present injector

Our injector is schematically shown in figure 2. The trailing edge has a lobed structure to promote rapid mixing. In the standard setup, H_2 is injected through the horizontal slots only. The design injection Mach number $M_{H_2} = 2.6$. In practice, this is probably not achieved because of deformation of the geometry through thermal expansion. Measurements of the true M_{H_2} are very difficult to perform due to the position of the injector in the chamber. Therefore, we chose $M_{H_2} = 1.0$ as an estimate for the numerical simulations. This is justified by the fact that we have sufficiently high hydrogen total pressure to allow for supersonic injection of the fuel and so the choice then represents a conservative estimate. In section 4.4 we show that a variation of M_{H_2} has little influence on the solution for $M_{H_2} \geq 1$. Our setup has auxiliary vertical slots, which are also shown in figure 2. These can be switched on if necessary to inject additional fuel into the chamber at Mach numbers $M_{H_2,aux}$. The advantages and disadvantages of this are discussed in section 4.2. A more detailed description of the injector and its performance is given by Gerlinger et al. [3].

3 NUMERICS

For the present investigation we used the commercial flow solver CFD++. The code is described in detail in the appropriate handbooks and so we only give a brief outline here. All fluxes are approximated to formally second order accuracy using cell centered variable storage. The simulations were steady and the discretized equation system was solved implicitly, which allowed a CFL of about 20. A multigrid approach was used for convergence acceleration. Hydrogen combustion was modeled by the modified 19-step, 9-species Jachimowski reaction scheme presented by Gerlinger et al. [4]. Nitrogen reactions are hereby neglected. We defined N_2 as the hidden species, due to its large mass ratio. Turbulence levels were prescribed at all inflows to $Tu = 2\%$, the ratio of turbulent to laminar viscosity was set to $\mu_t/\mu = 50$ and we used the SST turbulence model to close the RANS equations. However, the present method does not account for turbulence-chemistry interaction. We used wall functions to limit our computation times and carry out parameter studies in reasonable time frames. All walls were defined as isothermal due to the lack of detailed temperature measurements. For the channel walls, we set $T_{chan} = 400$K and for the injector walls $T_{inj} = 600$K. The effect of varying wall temperatures is discussed in section 4.4. The total temperature of the injected hydrogen was set to an estimated $T_{0,H_2} = 400$K and the total pressure, p_{0,H_2}, was varied to achieve the desired hydrogen mass flow rate and thus adjust the equivalence ratio. We exploited the symmetry of the setup and calculated only half of the domain. Also, we did not model the converging part of the Laval nozzle and instead assumed a sonic inflow at x=0. For all parameter studies we used a numerical grid, G1, with 1,056,928 hexahedrals. The parameters are varied individually from a reference operating point that features strong combustion at $T_{0,air} = 1400$K, $p_{0,air} = 4$bar and an equivalence ratio $\phi = 0.25$. The equivalence ratio is defined here as

$$\phi = \frac{\dot{m}_{H_2}}{\dot{m}_{H_{2,st}}}, \qquad (1)$$

where $\dot{m}_{H_2}$ is the actual global mass flow rate of hydrogen and $\dot{m}_{H_{2,st}}$ is the global mass flow rate of hydrogen that would be required for stoichiometric combustion. Finally, we compared the solution for the reference case on G1 with the respective solutions on two finer grids, G2 and G3, with 2,517,032 and 3,355,558 cells, respectively.

This allowed us to estimate the accuracy of the coarse grid solutions. We obtained G2 and G3 from G1 by successive grid refinements in selected regions. Since the grid size almost tripled in the process, this also led to a significant increase in computation time. However, we did not primarily refine G1 for the purpose of grid convergence studies. Rather, we attempted to lower residual levels and thus improve the solution, as will also be explained in the following.

4 RESULTS

4.1 Convergence

On all of the tested grids, it was difficult to achieve adequate drops in residual levels for strong combustion modes. Figure 3 shows the L^1 norm of the normalized residuals, $\|\mathbf{\Phi}^*\|$, for the primary governing equations, i.e. for the conservation of mass, momentum, energy and the turbulence quantities. The operating point is the reference case and the grid is G1.

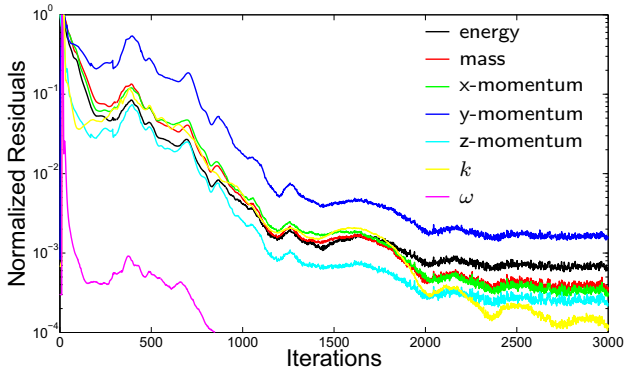

Figure 3: Primary residuals for grid G1, reference case

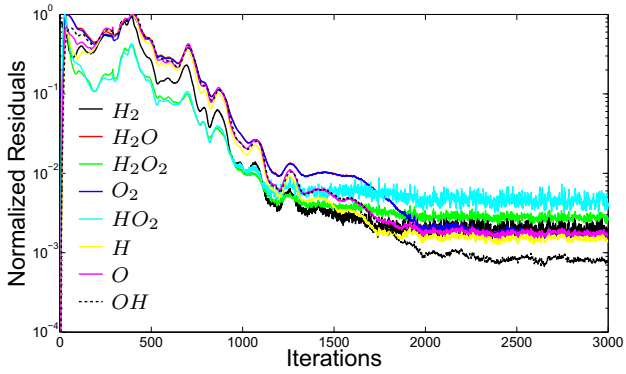

Figure 4: Species residuals for grid G1, reference case

The levels drop to $\|\mathbf{\Phi}^*\| < 2 \cdot 10^{-3}$, which is not entirely satisfactory. Convergence, as in all other calculations in this study, is reached after about 2500 iteration steps. The solution is essentially steady, but we note that it becomes unsteady if the mass flow rate is increased by increasing $p_{0,air}$ at the channel inflow while maintaining ϕ. Figure 4 shows the respective residuals for the species transport equations. Here, $\|\mathbf{\Phi}^*\| < 6 \cdot 10^{-3}$ and hence the situation is even less satisfactory than for the primary equations.

A closer investigation of the spatial distribution of $\mathbf{\Phi}^*$ (not shown here for brevity) indicates that the convergence problems mainly originate in the flame ignition region in the immediate wake of the injector. The residuals here are several orders of magnitude larger than in the rest of the flow field and are associated with large gradients in static temperature and high chemical activity.

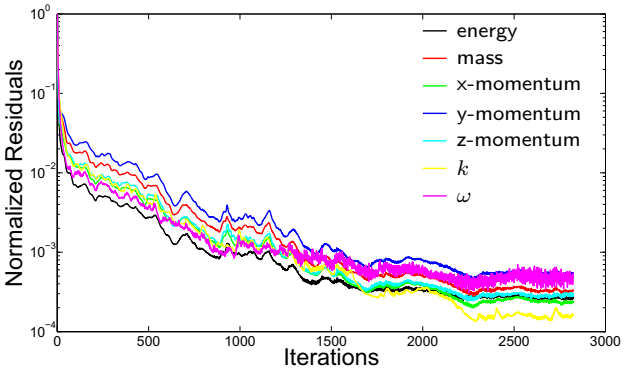

Figure 5: Primary residuals for grid G3, reference case

To improve convergence, we successively refined G1 in this area to obtain the finer grids G2 and G3. Figure 5 shows $\|\mathbf{\Phi}^*\|$ for the primary governing equations on G3. The situation has now improved with $\|\mathbf{\Phi}^*\| < 6 \cdot 10^{-4}$ and the spread in values is much smaller than before. For the species transport equations the improvement is even larger with $\|\mathbf{\Phi}^*\| < 7 \cdot 10^{-4}$, see figure 6. This is a reduction by almost one order of magnitude when compared to the solution on G1. However, even with the refined grid the convergence levels are not satisfactory. We would wish for a drop by at least another order of magnitude. The present data suggests that this could be achieved by an adequate further refinement of the grid. Our computational resources, however, do not at present allow for this if we wish to maintain reasonable runtimes.

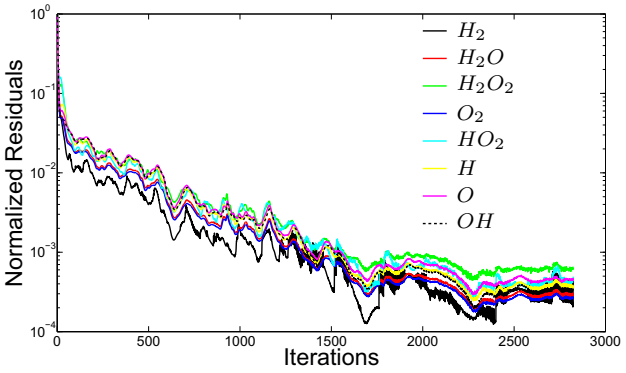

Figure 6: Chemical residuals for grid G3, reference case

The situation for weak combustion was somewhat better as long as the equivalence ratios are kept low. For

ϕ=0.09 the residuals for the primary equations were all $\|\mathbf{\Phi}^*\| < 7 \cdot 10^{-5}$ and for the species transport equations $\|\mathbf{\Phi}^*\| < 5 \cdot 10^{-4}$ on grid G1. With increasing ϕ and hence stronger chemical activity, the residuals grew. These results are also supported by the data of other researchers who observed similar convergence problems in related setups. For example, Yoon [5] achieves a drop in residual levels of three to four orders of magnitude for the case of transverse fuel injection into a supersonic flow when significant chemical activity is present. When chemical activity is low or absent, the drop in residual levels is higher. Goyne et al. [6] investigate a dual-mode supersonic combustor with ramp injection. For the residuals, they achieve a drop by four orders of magnitude. The present results are hence comparable to the data of similar numerical investigations published elsewhere. The convergence problems appear to be caused by the stiffness of the set of governing equations when chemical activity is significant. This view is supported by the decrease in residual levels for weak combustion modes and was also pointed out by Gerlinger et al. [3]. The latter introduced an adequate multigrid approach to improve the situation. We also tracked primary and conserved variables at various points in the wake of the injector. This data is not shown here for brevity, but it confirmed that the calculations usually converged after approximately 2500 iterations.

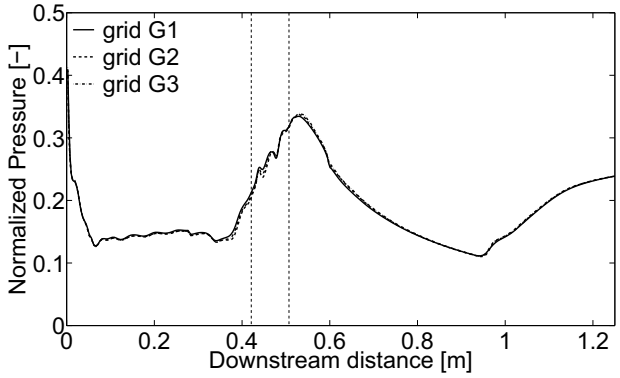

Figure 7: Normalized wall pressure for various grids

The different grids can be used to estimate the dependency of the results on spatial grid resolution. Since we are interested in comparing our numerical results with experimental data, this is best done by analyzing the calculated static wall pressure distributions on G1, G2 and G3. Figure 7 shows the corresponding data for the reference case described in section 3. Here, we plot static wall pressure as a function of downstream distance in the symmetry plane along the upper wall of the chamber, see also figure 1. The values are normalized by the total pressure of air, $p_{0,air} = 4$bar, at entry into the chamber. The two dashed vertical lines indicate the position of the leading and the trailing edges of the injector and so the second line is the injection point of hydrogen. The results on the different grids show little spread with the largest difference between G1 and G3 being about 6% at x=0.14m. We explain the various features of the curves in section 4.2. A further measure of quality can be obtained by comparing the fuel burnout ratios, η_b, for the different grids. This is defined here as the ratio of consumed fuel to injected fuel and is a function of downstream distance x. Similar measures of performance have been used by e.g. Lee [7]. For the present case

$$\eta_b(x) = 1 - \frac{\iint_A \rho_{H_2} u dy dz}{\dot{m}_{H_2,inj}} \qquad (2)$$

where A denotes integration over the whole cross sectional area and u is the axial velocity in x-direction. Our data for the different grids is shown in figure 8. The origin of the coordinate system is the point of hydrogen injection, x =0.507m. The differences between the results on G1 and G3 are less than 2% for x >0.55m. For x <0.55m, the differences between G1 and the finer grids are larger while G2 and G3 show virtually identical data over the whole range of x. The details of ignition and early combustion are hence captured more accurately on the finer grids while the results become similar further downstream when the combustion is well advanced. The shape of the curves is explained in more detail in section 4.2. The variations we found with varying mesh densities rendered G1 an acceptable choice when considering that runtimes on G3 were increased by a factor of six to seven.

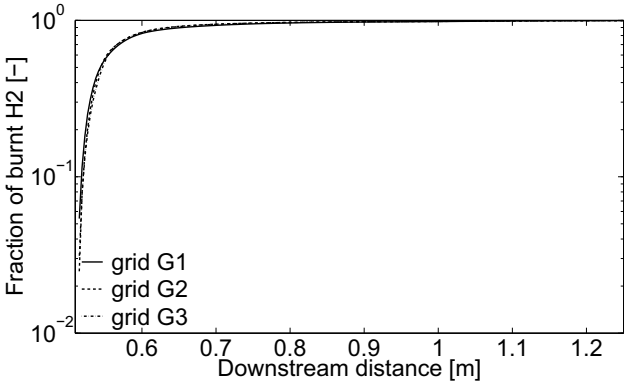

Figure 8: Hydrogen burnout ratios for various grids

4.2 Flow Features

Figures 9 (a), (b), (c) and (d) show the distributions of the Mach number, M, the axial velocity, u, the static temperature, T, and the mass fraction of OH, respectively, for various cross sections in the channel. The present coordinate system and the flow directions are also indicated for reference. In figure (a), we observe that the flow above and below the injector is largely subsonic. A core flow with M >1 is maintained after fuel injection and starts to grow after approximately half an injector length downstream of the injector trailing edge. At about one injector length downstream of the trailing edge almost the entire flow in the cross section becomes

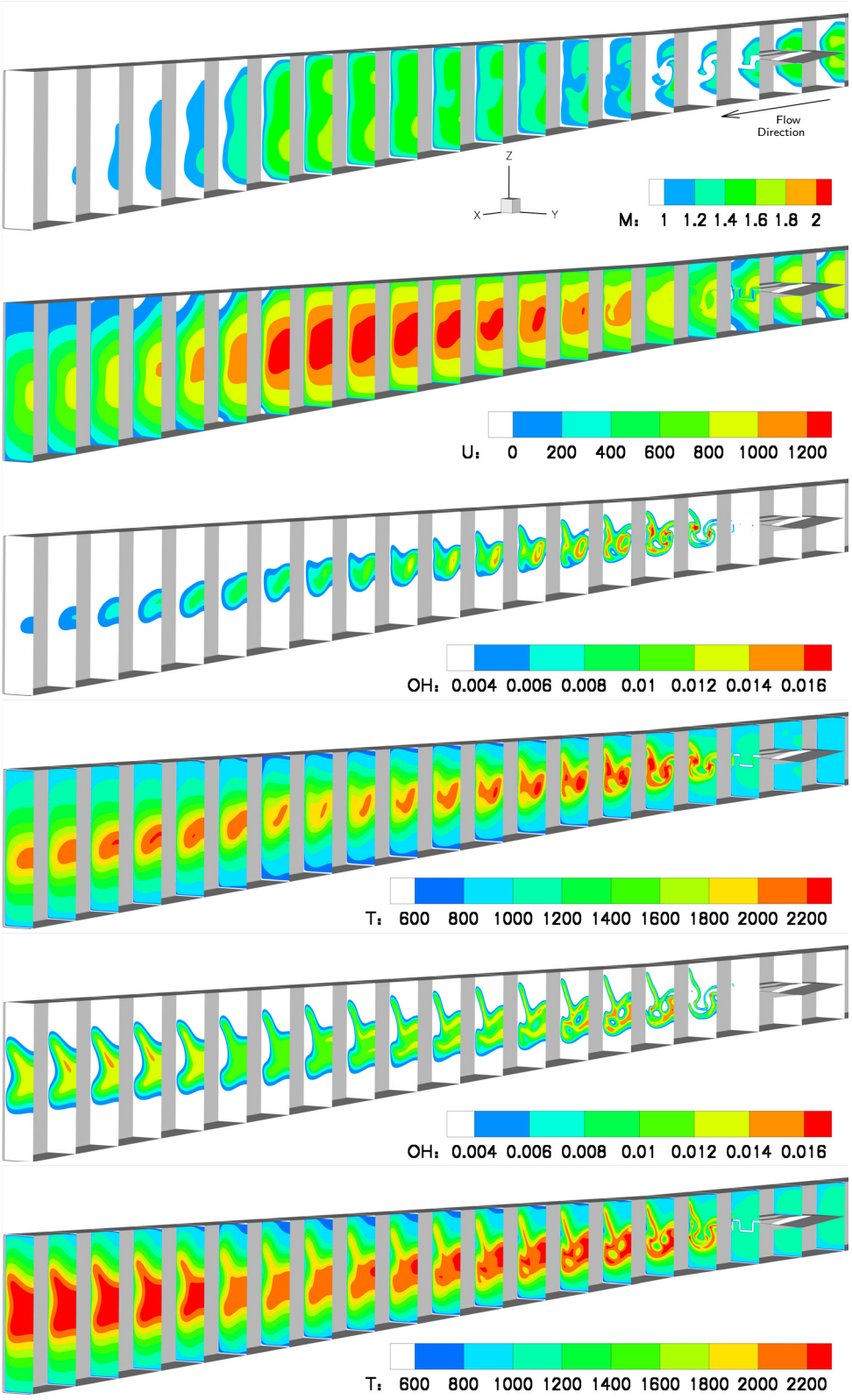

Figure 9: Distributions of (a) Mach number; (b) axial velocity u in [m/s]; (c) mass fraction of OH; (d) static temperature T in [K]; for the reference case in various cross sections in the channel. (e) mass fraction of OH and (f) static temperature T in [K] for auxuliary fuel injection through the vertical slots.

supersonic again for about two injector lengths. Further downstream, the effects of the overexpansion become visible and a shock train develops which decelerates the flow to subsonic speeds. At the exit, M <1 in the entire cross section. The shock train is associated with flow seperation and recirculation, which can clearly be seen in figure (b). There is a region of reversed flow in the corner between the upper wall and the sidewall for 0.95m< x <1.19m. A similar region develops in the corner between the lower wall and the sidewall but it is much smaller and extends between 0.97m< x <1.04m. There are also regions of reversed flow above and below the injector, which are due to both displacement effects and the combustion process itself. Generally, recirculation zones in supersonic flow are associated with total pressure losses and hence a decrease in overall system efficiency. However, we do note that for similar setups that we have investigated, the recirculation zones around the injector grow significantly smaller for sufficiently high Mach numbers. Similarly, the separation in the diverging part is only a result of the discharge into atmospheric conditions. At actual flight altitudes the associated recirculation zones disappear, as we will also show in the following. In addition, we find that the flow field is not symmetric for any of the variable distributions shown in figure 9. This is because there is no symmetry about the x-y-plane.

The distribution of OH provides an indication of where the regions with the most intense chemical activity are located. Our data indicates high concentrations of the radical in the immediate wake of the injector trailing edge, which is where the fuel-air mixture is ignited. The flame is hence very closely attached to the injector. This is exactly what one would aim for in a practical engine since it reduces the required overall engine length. Further downstream and in particular close to the channel exit, the concentrations of OH decrease significantly and we find that only minor chemical acticity in the central part of the combustion chamber remains. Closer to the injector, we observe high concentrations of OH close to the channel sidewall. From a comparison with part (d) of the figure, we find that these are associated with static temperatures in excess of 2200K which lead to high local heat loads on the walls and the injector trailing edges. This is problematic since it requires significant cooling of the structure in order to avoid material fatigue. To improve this situation, we injected auxiliary hydrogen through the vertical slots shown in figure 2 at $M_{H_2,aux}$=1. The mass flow rate per unit area, the total temperature and the total pressure were the same as for the other slots but this increased the overall equivalence ratio to ϕ=0.64. The distributions of the mass fraction of OH and the static temperature are given in figures 9 (e) and (f), respectively. The peak temperatures reached in the flame are now approximately T_{max}=2415K as opposed to T_{max}=2382K for the case with closed vertical slots. We observe that the flame structure changes significantly and the flame now occupies a much larger part of the cross sectional area than before. The regions of the largest OH concentration are now largely removed from the sidewall and pushed towards the center of the channel. Similar observations can be made for the temperature, but the effect is smaller here. We now also find stronger chemical activity further downstream which suggests that the hydrogen is not entirely consumed in the vicinity of the trailing edge, as before, but a significant part of it remains and only reacts in the shock train that develops in the vicinity of the exit. This interpretation is confirmed when analyzing the burnout ratios for hydrogen as a function of downstream distance after injection. This data is given in figure 10 for the reference case and for the case with auxiliary fuel injection. Clearly, the combustion efficiency is significantly lower in the latter case. The reason for this is probably two-fold. First, fuel in the vortex cores that develop in the wakes of the vertical ligaments remains trapped and is not transported and mixed with the oxygen from the main flow. Second, the local equivalence ratio is increased because the overall equivalence ratio is increased and it is harder to achieve adequate mixture of fuel and air within the combustor. Nevertheless, we note that the burnout ratios of the current design and in particular for the reference setup are surprisingly high. Approximately 90% of the fuel is consumed within two injector lengths after ignition. For an actual engine, this would allow a very short overall engine length. Based on the present results, we believe that it is possible to reduce the heat loads on the channel walls by injecting auxiliary fuel into the chamber but this can lead to a decrease in combustion efficiency for the present setup.

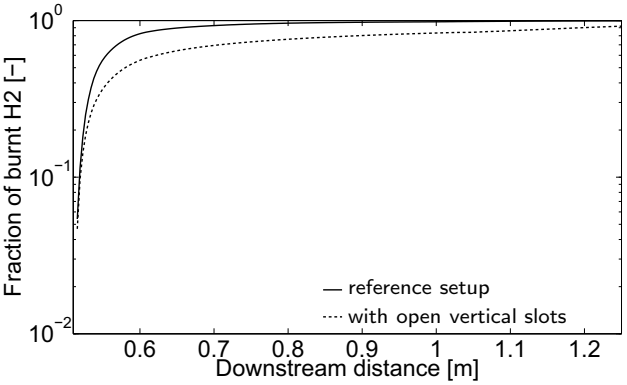

Figure 10: Hydrogen burnout ratios with and without auxiliary fuel injection

A further analysis of the flow field is possible from figure 11 where the axial velocity u in several cross sections around the injector is plotted. Here, x=0.421m is the location of the injector leading edge, while x=0.508m is 1mm downstream of the injector trailing edge. We observe that there are in fact two large pairs of regions of reversed flow in the channel corners. The first starts upstream of the injector leading edge and finishes around x=0.455m, which is a little upstream of the injector center. The second starts around x=0.473m and extends

past the injector trailing edge. While the first pair is probably caused by displacement effects of the injector, the second pair is associated with the combustion process itself. This interpretation is supported by the absence of the second recirulation regions in weak combustion mode. The corresponding plots are not given here for brevity, however. Additional recirculation zones develop in the wake of the vertical ligaments, as can be seen in the cross section at x=0.508m.

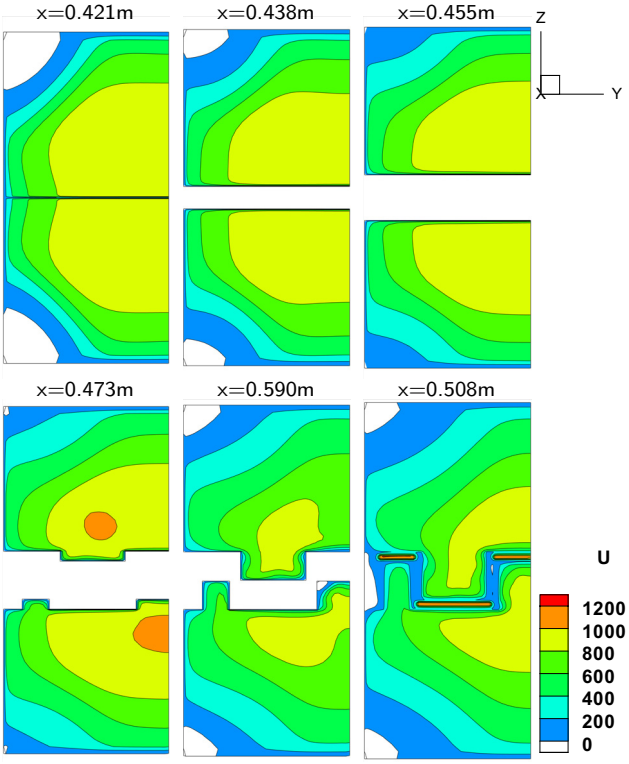

Figure 11: Axial velocity distributions u in [m/s] at various cross sections for the reference case

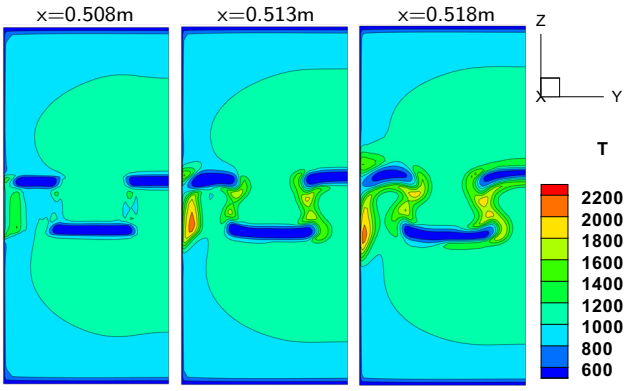

Figure 12: Static temperature distributions T in [K] at various cross sections for the reference case

It is now interesting to find the locations where the mixture ignites since this allows conclusions to be drawn with regard to the ignition process. Figure 12 shows data for the static temperature distribution in various cross sections in the immediate wake of the injector. As before, x=0.508m is located 1mm downstream of the trailing edge. We observe isolated peak temperatures in the wake of all vertical ligaments. These peaks indicate the locations where the combustion process is first initiated. A comparison with figure 11 shows that these correspond closely to the recirculation zones in the wake of the vertical ligaments. The flame then starts to grow to occupy an increasingly large region of the cross section. The mixture hence, strictly speaking, does not ignite in a supersonic flow but rather in subsonic regions that are the result of reversed flow in the wake of backwards facing steps. To clarify how hydrogen is transported into these regions, we plot the pathlines in the immediate vicinity of the injector trailing edge close to the wall. This data is given in figure 13, where the development of the recirculation zones is clearly visible. The pathlines are colored according to the local Mach number. In the recirculation zones, the air flow is reversed, the Mach number drops to subsonic speeds and the static temperatures rise. Hydrogen is transported into these regions by means of diffusion across the pathlines and subsequent convection into the recirculation zones. The ignition temperature of the mixture is reached since we have near stagnation point conditions and the combustion process is subsequently initiated.

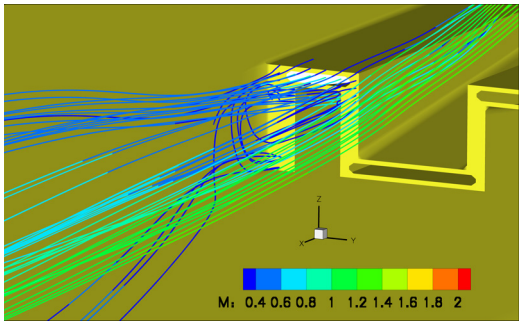

Figure 13: Pathlines in the wake of the injector close to the trailing edge. Pathline coloring is by local Mach number.

4.3 Comparison with Experimental Data

Figure 14 shows numerical and experimental static wall pressure distributions for the case of strong combustion at various equivalence ratios ϕ. Data is for the upper wall in the symmetry plane and as before, $T_{0,air} = 1400$K and $p_{0,air} = 4$bar. Numerical results are represented by lines, experimental data is represented by symbols and all pressures are normalized by $p_{0,air}$. The two vertical lines indicate the leading and trailing edges of the injector. We observe that our predictions match well with the experimental data inside the Laval nozzle, the isolator and in the wake of the injector up to $x \approx$0.94m. The main features of both the combustion process and the flow field should hence be captured adequately in these areas. However, there are noticeable differences right above the injector. From a comparison with the data given in section 4.2 we find that this coincides with the seperation and recirculation zones that develop on the

channel walls. Since we employ wall functions, it is likely that the size and strength of the separation bubbles are not captured accurately enough by our numerical solution, which would explain the observations. Similarly, we find discrepancies for $x > 0.94$m, where another separation zone develops due to the shock train. The numerical data predicts flow separation at $x \approx$0.94m while the experimental results suggest $x \approx$1.07m. As above, we believe that this is due to the use of wall functions. To show that the shock train is indeed an artefact of the discharge into ambient conditions, we also show the results for a back pressure of p_∞=1000Pa in figure 14. This data is marked by the index FL and the chosen back pressure correponds to the static presure in a standard atmosphere at an altitude of about 25km. The corresponding curve is lacking the steep increase in pressure around $x \approx$0.94m that the other numerical data shows. Instead, the pressure continues to drop smoothly, which is exactly what we would expect for an adapted or underexpanded channel. The decrease in back pressure also leads to a slightly increased pressure in the immediate wake of the injector and a somewhat altered shock train inside the isolator. Since there are regions of supersonic flow across the entire cross section of the diverging part of the channel in all cases, these results suggest a transport of information upstream via the boundary layer of the channel walls.

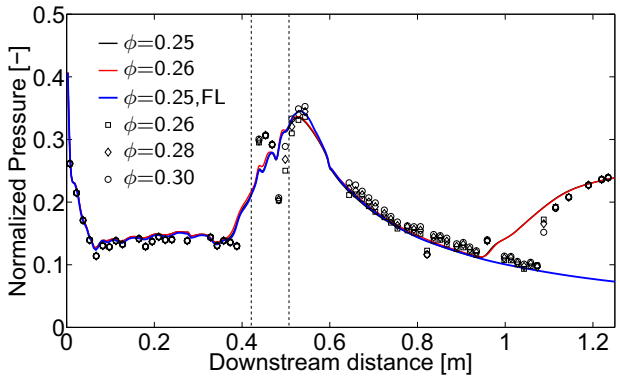

Figure 14: Normalized wall pressure for strong combustion at different equivalence ratios, numerics and experiment

Figure 15 shows numerical and experimental results for the case of weak combustion at various equivalence ratios ϕ. In addition, numerical data for the case of thermal choking at ϕ=0.52 is given. As before, numerical predictions are represented by lines while experimental data is indicated as symbols. Experimental data for the case of thermal choking is not available since the required mass flow rate of hydrogen cannot be delivered with the present experimental setup. We observe that for weak combustion the general trend is reproduced well. Differences exist only in the vicinity of the injector and for $x >$0.87m in the shock train. As before, this is probably due to flow separation in these regions and the use of wall functions. The pressure increase behind the injector is much lower than for the case of strong combustion. This is because combustion takes place almost exclusively in the shock train, where the flame is ignited due to the rise in static temperature.

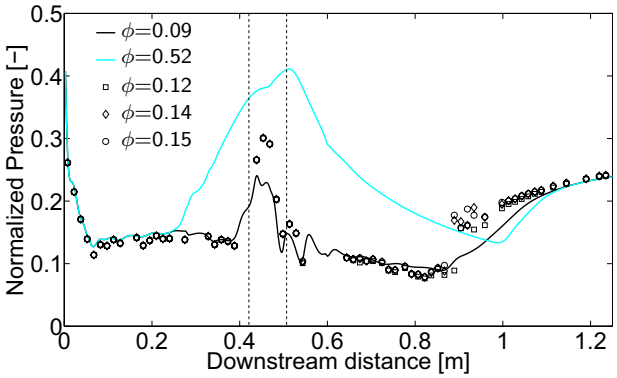

Figure 15: Normalized wall pressure for weak combustion at different equivalence ratios, numerics and experiment

A comparison of figures 14 and 15 shows that the combustion process and in particular the combustion mode significantly influence regions upstream of the hydrogen injection point. For example, when compared to weak combustion, the static wall pressures in strong combustion modes are increased in regions upstream of the injector trailing edge. The situation is even more pronounced for the case of thermal choking, ϕ=0.52, where we find a large pressure increase that extends upstream until approximately the center of the isolator. This increase is due to the formation of a shock structure in the isolator, which is the result of excessive heat addition during the combustion process. For $x >$0.25m the flow is then mostly subsonic and the losses associated with this combustion mode are much higher than for the case of strong combustion.

4.4 Burnout Ratios and Parameter Variations

Figure 16 compares the burnout ratios for a range of different equivalence ratios ϕ and all combustion modes that have been analyzed during the present study. The first observation we make is that, for strong combustion, represented here by ϕ=0.25 and ϕ=0.26, the combustion efficiency decreases slightly with increasing ϕ. One reason for this might be that an increase in the overall equivalence ratios also leads to an increase in the local equivalence ratios and hence can have negative effects on the mixing behavior of the injector, i.e. the mixing times between fuel and oxygen are increased. For a discharge into conditions at a realistic flight level, marked by the index FL, we observe a slight increase in efficiency. The reasons for this are, at present, unclear and require further investigation.

For the case of weak combustion, ϕ=0.09, the burnout ratios are significantly decreased compared to the other combustion modes and most of the fuel is consumed within the shock train of the diverging section of the

channel. This combustion mode is highly undesirable because, in real flight conditions, it would lead to blow off and engine failure. The case of thermal choking, ϕ=0.52, shows combustion efficiencies well below the strong combustion mode but better than for weak combustion. However, since this mode is associated with a shock system that develops upstream of the injector, it leads to significant losses in total pressure and is hence also undesirable in real flight conditions.

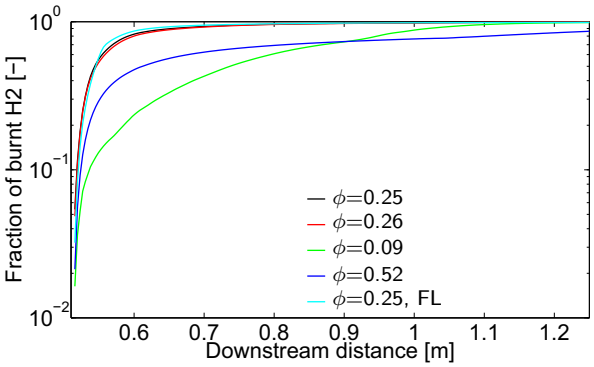

Figure 16: Hydrogen burnout ratios for variable ϕ and different combustion modes

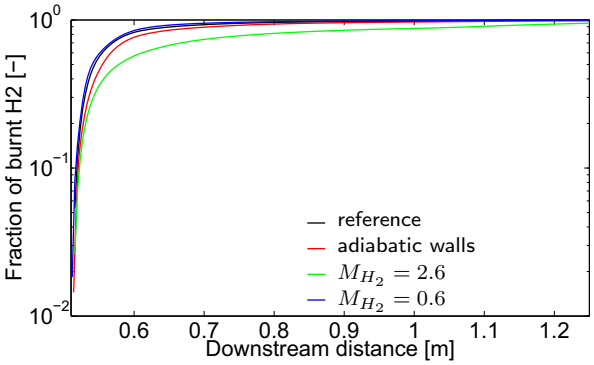

Figure 17: Hydrogen burnout ratios for several parameter variations

Figure 17 shows the burnout ratios for the reference case, for the case of adiabatic walls, for the case of hydrogen injection at the design Mach number M_{H_2}=2.6 and for subsonic injection of hydrogen at M_{H_2}=0.6. Each of these parameters is varied individually, i.e. all other parameters remain as chosen for the reference case and given in section 3. First, we observe that the combustion efficiency is reduced if the walls are adiabatic. This suggests that it is beneficial to cool the channel walls to allow for an improved consumption of the injected fuel. In addition, we find that the efficiency is somewhat improved if the injection Mach number is at the design value of M_{H_2}=2.6. The difference to the reference case in consumed fuel is on the order of 5% within a distance of about one injector length downstream of the injector trailing edge and quickly reduces to approximately 2% for larger distances. For subsonic injection, however, the efficiency drops significantly with a maximum difference of about 20% in the amount of consumed fuel at x=0.60m. The data therefore suggests that variations in hydrogen injection Mach numbers have no significant effects on combustion efficiencies so long as M_{H_2} remains supersonic but that we can expect significant losses in performance for a subsonic injection.

5 CONCLUSIONS

The present calculations suggest that it is possible to carry out parameter studies for a model scramjet combustion chamber with commercial CFD packages in reasonable runtimes and on rather coarse meshes. The disadvantages are, as can reasonably be expected, the reduced accuracy and, probably, reliability of the solution. Nevertheless, a comparison with experimental data showed reasonable agreement with simulations. In addition, trends were predicted adequately and the numerics could reproduce all combustion modes found in the experiments. A sensible approach would therefore be to use a coarse grid for the initial layout of a model engine and subsequently improve the design using more sophisticated approaches. One future aim of our work is to reduce the computional domain to a smaller geometric size. This would allow us to increase the mesh density in the remaining domain while maintaining reasonable runtimes and we can then integrate the governing equations to the wall. These measures aim at improving the predictions for the size and strength of the recirculation regions as well as the chemical processes in the flame ignition region. The latter is expected to also lead to improved convergence rates. In addition, a range of additional parameter studies will be interesting. This includes variations in air total temperature and total pressure as well as one example with stagnation values that would be typical for actual flight conditions.

ACKNOWLEDGEMENTS

The present work has been carried out under a research grant from the German Research Foundation (DFG) within the framework of the research training group GRK1095/1. This support is gratefully acknowledged. The authors would also like to thank Fabian Kroll for his support with some of the calculations.

References

[1] B. Weigand, U. Gaisbauer, B. Reinartz, H.-P. Kau, and W. Schröder. Das Graduiertenkolleg 1095/1: Aero-Thermodynamische Auslegung eines Scramjet - Antriebssystems für zukünftige Raumtransportsysteme. In *DGLR-2006-127*. DGLR Jahrestagung, 2006.

[2] Chun, J. and Scheuermann, T. and von Wolfersdorf, J. and Weigand, B. Experimental study on combustion mode transition in a scramjet with parallel in-

jection. In *14th AIAA/AHI Space Planes and Hypersonic Systems and Technologies Conference*. AIAA 2006-8063, 2006.

[3] P. Gerlinger, P. Kasal, F. Schneider, J. von Wolfersdorf, B. Weigand, and B. Aigner. *Basic Research and Technologies for Two-Stage-to-Orbit Vehicles*. Wiley-VCH Verlag GmbH & Co. KGaA, 2005.

[4] P. Gerlinger, H. Möbus, and D. Brüggemann. An Implicit Multigrid Method for Turbulent Combustion. *Journal of Computational Physics*, 167:247–276, 2001.

[5] S. Yoon. Calculation of Supersonic Combustion Using Implicit Schemes. *AIAA Journal*, 42(12):2482–2489, December 2004.

[6] C.P. Goyne, C.G. Rodriguez, and C.R. McClinton. Experimental and Numerical Study of a Dual-Mode Scramjet Combustor. *Journal of Propulsion and Power*, 22(3):481–489, December 2006.

[7] S.-H. Lee. Characteristics of Dual Transverse Injection in Scramjet Combustor, Part 2: Combustion. *Journal of Propulsion and Power*, 22(5):1020–1026, 2006.